Spin dynamics of the magnetocaloric compound $MnFe_4Si_3$

N. Biniskos,[1,2] S. Raymond,[2] K. Schmalzl,[1] A. Schneidewind,[3] J. Voigt,[4] R. Georgii,[5] P. Hering,[4]
J. Persson,[4] K. Friese,[4] and T. Brückel[3,4]

[1]*Jülich Centre for Neutron Science, Forschungszentrum Jülich GmbH, Outstation at ILL, BP 1 56, 38042 Grenoble, France*
[2]*Université Grenoble Alpes, CEA, INAC, MEM, 38000 Grenoble, France*
[3]*Jülich Centre for Neutron Science at Heinz Maier-Leibnitz Zentrum, Forschungszentrum Jülich GmbH, Lichtenbergstrasse 1, 85747 Garching, Germany*
[4]*Jülich Centre for Neutron Science and Peter Grünberg Institut PGI, JARA-FIT Forschungszentrum Jülich GmbH, 52425 Jülich, Germany*
[5]*Heinz Maier-Leibnitz Zentrum und Physik Department E21, Technische Universität München, Lichtenbergstrasse 1, 85748 Garching, Germany*

(Received 11 July 2017; published 6 September 2017)

The magnetic excitation spectrum of the magnetocaloric compound $MnFe_4Si_3$ has been investigated by means of polarized and unpolarized inelastic neutron scattering on single crystals. Spectra were collected in the ferromagnetic phase ($T_C \approx 305$ K), as well as in the paramagnetic state, in order to understand the nature of the magnetism in $MnFe_4Si_3$. Spin-wave measurements at 1.5 K reveal a strong anisotropy of the magnetic exchange interactions along the (h00) and (00l) reciprocal directions of the hexagonal system, which also manifests itself in the q-dependent linewidths in the paramagnetic state. The correlation lengths indicate a short-range order, while the average linewidth is of the order of $k_B T_C$ pointing to a behavior typical of many ferromagnets. In addition, the in- and out-of-plane spin fluctuations are found to be isotropic around T_C and can be suppressed by a magnetic field of 2 T.

DOI: 10.1103/PhysRevB.96.104407

I. INTRODUCTION

One possibility for an environmentally friendly and more efficient use of energy in daily life is the use of magnetic refrigeration technologies, which are based on the magnetocaloric effect (MCE) [1]. MCE is the reversible temperature change of a magnetic material upon the isothermal application of a magnetic field and its adiabatic removal [2]. Since the early demonstration of magnetocaloric (MC) cooling near room temperature in the ferromagnetic (FM) material gadolinium [3] and the more recent discovery of giant MCE in $Gd_5Si_2Ge_2$ [4], the research publications on MC cooling have increased greatly. Nowadays, a significant number of materials with magnetic phase transition near room temperature have been proposed for applications [5,6]. Such materials should combine a high adiabatic temperature change (ΔT_{ad}) with a large isothermal entropy change (ΔS_{iso}). In addition, a good candidate material should consist of environmentally friendly, abundant, low-cost, and nontoxic elements.

Among the suggested MC compounds for applications, the $Mn_{5-x}Fe_xSi_3$ ($0 \leqslant x \leqslant 5$)-based systems exhibit moderate MCE at low magnetic fields and at different temperatures depending on x [7]. Early studies reported that they crystallize in a hexagonal structure with the space group $P6_3/mcm$, with two distinguished crystallographic sites—Wyckoff positions (WP) $6g$ and $4d$—occupied by Mn and Fe in different ratios depending on composition [8]. From this series, $MnFe_4Si_3$ is a promising candidate material since a transformation from the paramagnetic (PM) state to the FM phase occurs at the Curie temperature (T_C) ≈ 300 K [9–11] with $\Delta S_{iso} \approx 2$ JK^{-1}kg^{-1} for a field change from 0 to 2 T [7,9]. The order of the FM transition seems not to be fully established. Hysteresis loops point to a first-order FM transition [9]. Recent measurements of hyperfine fields with Mössbauer spectroscopy propose that the type of the magnetic transition cannot be strictly characterized as first or second order [12]. In this framework, it is worthwhile to note that, in Fe_2P-based MC materials, the order of the FM transition changes from first to second order depending on composition [13].

According to recent x-ray and neutron diffraction experiments performed on single crystals of $MnFe_4Si_3$, a partial ordering of Mn and Fe atoms was observed on the sites of mixed occupancy, which leads to reduction of symmetry from space group $P6_3/mcm$ to $P\bar{6}$ [9]. For the present experimental study, the higher symmetric $P6_3/mcm$ structure [8] proved to be a sufficient approximation. In this structure (see Fig. 1), the WP $4d$ is occupied by Fe atoms surrounded by six Si atoms at a distance $\approx$2.4 Å in the form of a distorted octahedra [$FeSi_6$]. The WP $6g$ has a mixed occupancy of Fe-Mn (Fe occupancy $\approx$67%, Mn occupancy $\approx$33%) and forms triangular units in the ab plane (interatomic distance $\approx$2.775 Å). The triangular units are stacked along the c direction, forming empty distorted $[MnFe]_6$ octahedra. The magnetic moments on the WP $6g$ lie in the basal plane of the hexagonal system with a magnitude of 1.5(2) μ_B, while no significant magnetic moment could be determined on WP $4d$ [9]. The direction of the magnetic moments is consistent with magnetization measurements performed on single crystals, where a strong anisotropy is found with the easy axis of magnetization lying perpendicular to the c axis [9].

MCE potentially occurs in any magnetic ordering process. Although different scenarios are well-known for specific systems, no microscopic mechanism based on key ingredients such as coupling of spin, lattice, and electronic degrees of freedom has been experimentally proven. Inelastic Neutron Scattering (INS) measurements, which microscopically probe the magnetization dynamics, can tackle this question and shed light onto the fundamental mechanism of MCE. To this aim, the spin dynamics of the MC compound $MnFe_4Si_3$ have been investigated above and below T_C as a function of the wave

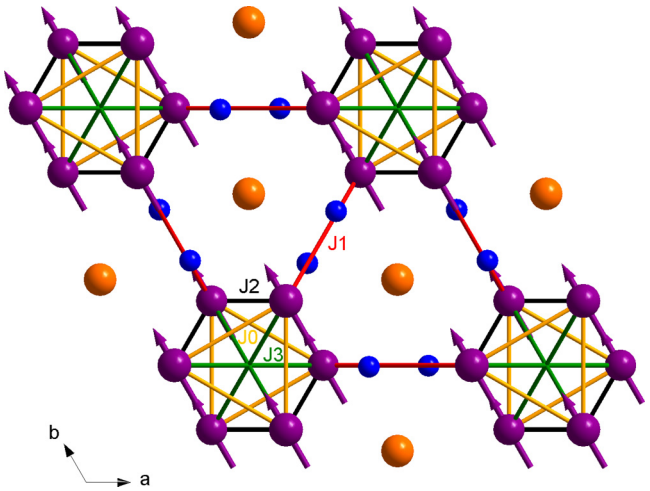

FIG. 1. Projection on the hexagonal plane of the crystal structure of $MnFe_4Si_3$ in $P6_3/mcm$ space group. Sites occupied by Mn and Fe (WP 6*g*, large magenta) carry magnetic moments 1.5 μ_B parallel to *b* axis; sites occupied by Fe (WP 4*d*, large yellow) and Si atoms (small blue) carry no magnetic moments. Yellow lines (J_0) connect atoms in the same plane, red lines (J_1), black lines, (J_2), and green lines (J_3) in different planes.

vector **Q** and the energy E. This compound is a suitable candidate for detailed INS experiments, since large single crystals can be grown [9].

II. EXPERIMENTAL DETAILS

The single crystal of $MnFe_4Si_3$ was grown by the Czochralski method [9] and two samples of this batch with a mass of about 7 g each were mounted on an aluminium sample holder and oriented in the (a*,c) and (a*,b*) scattering plane of the hexagonal lattice, respectively. The linewidths of the Rocking curve of each sample consist of a single Gaussian peak and is of about 0.3 degrees as measured by neutron scattering.

INS measurements were carried out on the cold and thermal triple-axis spectrometers (TAS) IN12 [14] and IN22 at the Institut Laue Langevin, as well as on MIRA [15] and PUMA [16] at the Heinz Maier-Leibnitz Zentrum. The spectrometers used for INS studies were set up in W configuration with a fixed final energy and a fully focusing setup. MIRA was used in elastic TAS mode with 60′ secondary collimation. The corresponding integration in energy covers the range from −0.1 to 0.1 meV. Additional information regarding each configuration is given in Table I.

For unpolarized INS measurements below T_C, the sample was cooled down to the base temperature $T \approx 1.5$ K with an orange or closed-cycle cryostat (configurations A and B in Table I) while, for measurements above T_C, a cryofurnace was used to cover the temperature region of $80 \leqslant T \leqslant 500$ K (configuration C in Table I). Elastic measurements on MIRA were performed using a 2.2 T vertical field magnet with the field applied in the plane (configuration F).

For INS measurements with polarized neutrons, the incident neutron beam spin state was prepared for IN12 with a transmission polarizing cavity [14] located after the velocity selector and for IN22 with a Heusler monochromator. All along the neutron path, guide fields were installed to maintain the polarization of the beam. In order to investigate the spin-wave scattering, the sample was placed in a 2.5 T vertical field magnet. The single crystal was first heated up above T_C to 316 K and then cooled down to 1.5 K under a vertical magnetic field of $H_z = 1$ T applied parallel to the *b* axis of the hexagonal system of the sample, corresponding to an axis within the easy plane of magnetization [9]. This results in a single domain state of the sample. The scattered beam was analyzed by a combination of a Mezei spin flipper and a horizontally focusing Heusler analyzer set at fixed k_f (configurations D and E in Table I). The PM scattering was also investigated in detail at $T = 316$ K using the spherical polarization analysis setup CRYOPAD and configuration E. For all measurements with polarized neutron beam (configurations D and E), a flipping ratio of about 14 has been measured on a graphite sample.

TABLE I. Instrument configurations. "PG(002)" and "Heusler" refer to pyrolytic graphite and $Cu_2MnAl(111)$, respectively. Higher order contamination was removed using a PG filter in the scattered neutron beam on IN22 and PUMA. On IN12 and MIRA a velocity selector (VS) was employed before and a cooled Be filter after the monochromator, respectively. The symbol " * " refers to polarized setups.

Config.	TAS	Monoch.	Anal.	k_f (Å^{-1})	Filter
A	IN12	PG(002)	PG(002)	2	VS
B	PUMA	PG(002)	PG(002)	1.971	PG
C	IN12	PG(002)	PG(002)	1.3	VS
D	IN12*	PG(002)	Heusler	2	VS
E	IN22*	Heusler	Heusler	2.662	PG
F	MIRA	PG(002)	PG(002)	1.4	Be

III. SPIN-WAVE SCATTERING

Magnetic excitations were measured around the zone centers $\boldsymbol{\tau} = (2, 0, 0)$, $\boldsymbol{\tau} = (0, 2, 0)$, and $\boldsymbol{\tau} = (0, 0, 2)$ with configuration A and B [17]. There, the calculated magnetic form factors for Fe and Mn are expected to have significant magnitude. To extract acoustic magnon branches, constant energy and constant **Q** scans were carried out at energy transfers below 20 meV at $T = 1.5$ K along the high symmetry reciprocal directions (h00), (hh0), and (00l) of the hexagonal system. Specific scans were repeated above T_C, e.g., at $T = 313$ K, in order to establish the magnetic nature of the excitations. Typical representatives of such measurements are shown in Fig. 2 at $\mathbf{Q} = (2.3, 0, 0)$, where the peak observed at $T = 1.5$ K is replaced by a broad quasielastic signal above the ordering temperature at $T = 313$ K.

Further experiments with polarized neutrons were performed along the (h00) and (00l) directions at 1.5 K using instrument configurations D and E. Figure 3 shows a characteristic constant energy scan performed for an energy transfer of 5 meV where the peak observed in the spin flip (SF_{zz}) channel vanishes in the non-spin flip (NSF_{zz}) channel (see Appendix A). Measurements with polarized neutrons are crucial in such a ferromagnet as acoustic phonon, and magnon modes originate from the same Brillouin zone center.

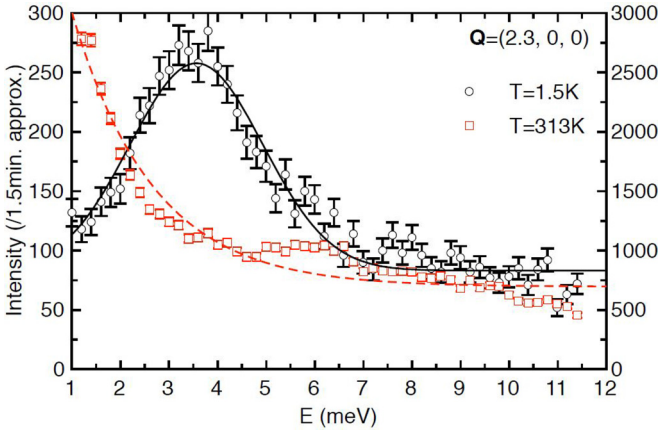

FIG. 2. Energy spectra at $\mathbf{Q} = (2.3, 0, 0)$ measured at IN12 spectrometer with unpolarized setup at 313 K (squares) and 1.5 K (circles). Neutron intensity for data at 1.5 K and 313 K is given on the left and right vertical axis, respectively. The solid line corresponds to a Gaussian function fit and the dashed line is a guide for the eyes.

Moreover, all spectra were examined carefully for spurious scattering, especially aluminium and copper contamination, and the corresponding regions were masked during the data evaluation. Magnetic excitations, both for the constant $\mathbf{Q}$ (Fig. 2) and constant E (Fig. 3) scans, were fitted with Gaussian functions.

The obtained magnon dispersion along the main three symmetry directions [(h00), (00l), and (hh0)] is shown in Fig. 4. While the magnon branches are found to be rather isotropic in the two basal plane directions, (h00) and (hh0), a much steeper dispersion develops along (00l). The experimental spin-wave spectrum at low energies ($E \leqslant 5$ meV) can be described by a quadratic dispersion, $E = \Delta + D_{(hkl)}q^2$, where Δ is the energy gap, $D_{(hkl)}$ is the spin-wave stiffness, and q is the momentum transfer. The obtained values are $\Delta = 0.71(25)$ meV, $D_{(h00)} \simeq D_{(hh0)} = 43(7)$ meVÅ^2, and $D_{(00l)} = 310(30)$ meVÅ^2 for the in- and out-of-plane magnon

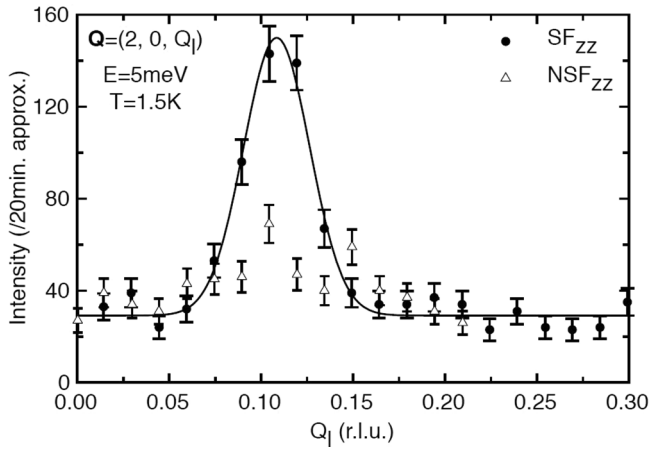

FIG. 3. Polarized inelastic neutron scattering spectra obtained at IN12 around $\mathbf{Q} = (2, 0, Q_l)$ at constant energy transfer of 5 meV at $T = 1.5$ K from spin flip and non-spin flip channel. The solid line represents a fit with a Gaussian function.

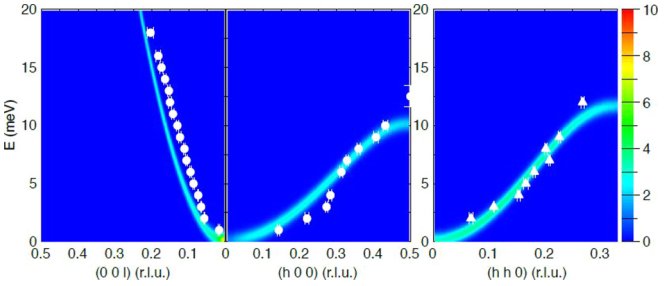

FIG. 4. Magnon dispersion at $T = 1.5$ K along (00l), (h00), and (hh0) directions from polarized (circles) and unpolarized (triangles) INS measurements. The color-coded intensity corresponds to spin-wave simulation as described in the text.

branch, respectively. However, the obtained value for the spin gap is within the instrument resolution, which is approximately 0.5 meV for configuration A.

To describe the spin-wave spectrum, and to extract the relevant exchange interactions of this compound, the SpinWave software package was used [18]. Since our experimental data revealed only the lower energy acoustic magnon dispersion for each direction, a simplified spin model was employed. Given the experimental uncertainty on the magnetic moment on the 4d site [9], we considered one type of magnetic atoms carrying a spin S on the 6g sites of mixed occupancy. As no significant differences are observed between the dispersion measured along the (h00) and (00l) directions at zero field and for $H = 1$ T applied along the b axis, we assume for simplicity that the magnetic moments are lying along the b axis. Furthermore, the Zeeman effect is negligible, being of the order of 0.09 meV for a magnetic moment of 1.5 μ_B under a magnetic field of 1 T. The spin model is described by a Heisenberg-type Hamiltonian, $H_H = \sum_{i,j} J_{ij} S_i S_j$, where J_{ij} denotes the exchange couplings between sites i and j.

The exchange interactions between the nearest neighboring magnetic atoms located at WP 6g are shown in Fig. 1 and are described in Table II. First, the coupling between magnetic atoms in the same distorted $[MnFe]_6$ octahedra are considered. This concerns $2SJ_0$, the exchange between the spins located on a triangle (distance 2.775 Å), $2SJ_2$ and $2SJ_3$ that couples two spin located on adjacent triangles separated by $c/2$ with distances 2.885 and 3.981 Å, respectively. Second, the exchange $2SJ_1$ concerns the shortest distance (4.304 Å) between spins located on adjacent distorted $[MnFe]_6$ octahedra. The

TABLE II. Exchange constant values, number of neighbors between magnetic sites (z_n), in-plane (IPP), and out-of-plane projections (OPP) of the vector linking the magnetic sites and distances between magnetic atoms (see Fig. 1). The symbol "−" means that the exchange interactions cannot be determined in the present work.

Exchange	Value (meV)	z_n	IPP	OPP	Distance (Å)
$2SJ_0$	−	2	0.409	0	2.775
$2SJ_1$	−4	2	0.528	0.5	4.304
$2SJ_2$	−18	4	0.236	0.5	2.855
$2SJ_3$	−	2	0.472	0.5	3.981

experimental fact that the magnon dispersion is much steeper along the (00l) direction than in the basal plane, imposes that the exchange interaction with the highest ratio of out-of-plane to in-plane component, $2SJ_2$, is the dominant one. The second most important interaction concerning acoustic spin waves is the one that connects the different octahedra, $2SJ_1$, which is mandatory to create the in-plane dispersion. The calculated dispersion using only the $2SJ_1$ and $2SJ_2$ interactions with the values indicated in Table II is shown in Fig. 4. This simplified model describes well the experimental dispersion; including further interactions is not relevant, given the present set of data. In this respect, it should be pointed out that $2SJ_0$ does not participate in the out-of-plane dispersion by nature. Our simulations show further that it does not contribute to the in-plane acoustic modes but only to the optic modes. Since these modes were not experimentally observed in the present study, $2SJ_0$ cannot be determined. In addition, it is found that the effect of $2SJ_3$ is redundant with the one of $2SJ_1$ and $2SJ_2$ and cannot be disentangled.

IV. PARAMAGNETIC SCATTERING

The spin dynamics of the MC compound $MnFe_4Si_3$ in the PM state was investigated with INS measurements, which were carried out with the scattering vectors along the (h00) and (00l) directions. For determining the extent of the spin fluctuations in the PM region, spectra have been collected with an unpolarized neutron beam at small q, using instrument configuration C. The measured intensity was corrected by the Bose factor and a constant background was subtracted so that the obtained results correspond to the imaginary part of the dynamical spin susceptibility $\chi''(\mathbf{Q},\omega)$. A typical temperature dependence for $\mathbf{Q} = (0.25, 0, 0)$ for an energy transfer of $E = 0.3$ meV is shown in Fig. 5. The spin fluctuations show their maximum at T_C and extend for temperatures higher than $1.5T_C$. The inset in Fig. 5 shows the temperature dependence of the beam polarization P. Measurements were performed with the use of

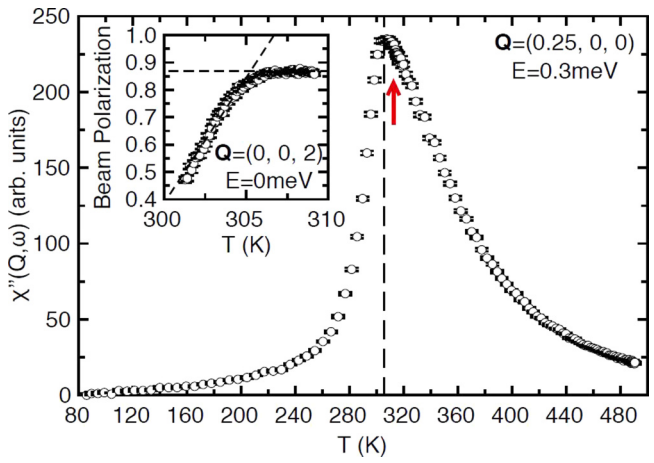

FIG. 5. Temperature dependence of dynamical spin susceptibility $\chi''(\mathbf{Q},\omega)$ at $\mathbf{Q} = (0.25, 0, 0)$ and $E = 0.3$ meV measured with unpolarized neutrons at IN12. The dashed vertical line and the red arrow indicate $T_C \approx 305$ K and $1.036T_C \approx 316$ K, respectively. The inset shows the temperature dependence of the beam polarization at $\mathbf{Q} = (0, 0, 2)$ Bragg peak.

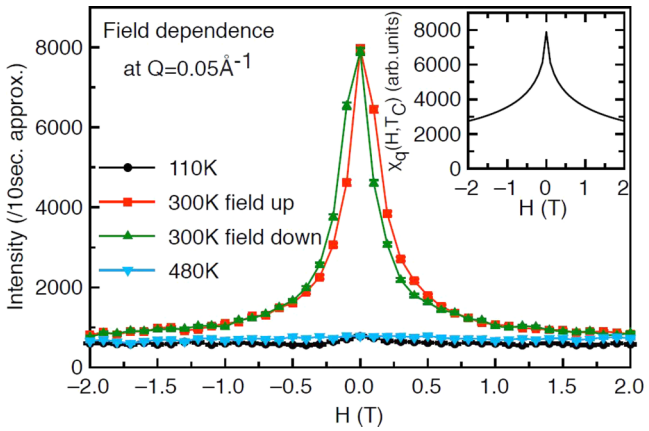

FIG. 6. Evolution of elastic scattering at $Q = 0.05$ Å^{-1} measured at MIRA as a function of magnetic field at three temperatures. Lines can be used as guides for the eyes. The inset shows a calculation of the field dependence of $\chi_q(H,T_C)$ following Ref. [19].

CRYOPAD and configuration E in non-spin flip NSF_{xx} and spin flip channel SF_{xx} at the $\mathbf{Q} = (0, 0, 2)$ Bragg peak. The calculated beam polarization was obtained by:

$$P = \frac{NSF_{xx} - SF_{xx}}{NSF_{xx} + SF_{xx}}. \quad (1)$$

It is clearly seen that a considerable beam depolarization occurs for $T \leqslant T_C$ due to the magnetic domain structure, indicating the transition from the PM state to the FM phase at $T_C = 305$ K.

Figure 6 shows the evolution of elastic scattering measured with configuration F as a function of magnetic field at three temperatures: close to T_C, above T_C, and below T_C at the lowest accessible Q range. In this very low Q range, the contribution to the intensity in the obtained spectra is attributed mainly to magnetic scattering. Consistently with Fig. 5, the magnetic scattering is significantly reduced at 110 and 480 K compared to 300 K. Around the critical temperature, a field of 2 T is sufficient to suppress the magnetic fluctuations. The spectra at 300 K for ramping the magnetic field in a positive or negative direction are offset by the coercive field (≈0.03 T). To get a qualitative description of the suppression of the magnetic fluctuations, the model of Ref. [19] was used and the calculated q-dependent susceptibility at T_C as a function of field is shown in the inset in Fig. 6 (see Discussion).

To get insight into the spin dynamics near room temperature and above T_C, the PM scattering was studied at $T = 316$ K corresponding to $1.036 \times T_C$ along the (h00) and (00l) directions with constant $\mathbf{Q}$ scans using instrument configuration E. Spectra were collected in two non-spin flip channels NSF_{yy} and NSF_{xx} around the $\boldsymbol{\tau} = (2, 0, 0)$ and $\boldsymbol{\tau} = (0, 0, 2)$ zone centers. The magnetic fluctuations were extracted by taking the difference of intensity of the two non-spin flip channels taking into account higher order corrections of the monitor counts of each polarization channel. This gives access to the spin fluctuations along the c axis, $\langle \delta M_c \rangle$ (see Appendix A). A typical measurement is depicted in Fig. 7, where energy scans at $\mathbf{Q} = (2.2, 0, 0)$ and $\mathbf{Q} = (2.3, 0, 0)$ are shown. As expected, the intensity decreases when q increases. The obtained spectra were convoluted with the 1D-instrument resolution and values

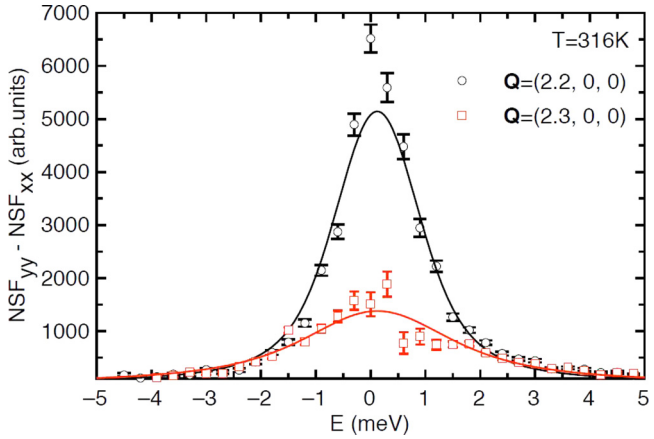

FIG. 7. Spin fluctuations $\langle \delta M_c \rangle$ obtained at IN22 and measured at $\mathbf{Q} = (2.2, 0, 0)$ (black circles) and $\mathbf{Q} = (2.3, 0, 0)$ (red squares) at $1.036 T_C$. Solid lines represent fits as explained in the text.

for the q-dependent susceptibility χ_q and linewidth Γ_q were extracted as described in Appendix B.

The obtained values for χ_q and Γ_q for (00l) and (h00) directions at 316 K are shown in Fig. 8. χ_q decreases faster along the (00l) direction compared to (h00), indicating a shorter inverse correlation length. A Lorentzian fit for the q-dependent susceptibility χ_q gives values for the inverse correlation lengths κ_q: $\kappa_{(00l)} = 0.054(3)\,\text{Å}^{-1}$ and $\kappa_{(h00)} = 0.14(1)\,\text{Å}^{-1}$. The energy range of the spin fluctuations is of the same order of magnitude as the one of the spin waves along these high symmetry directions. For $q = 0$ the linewidth extrapolates to zero. To describe the experimental data for Γ_q at $1.036 T_C$, two different

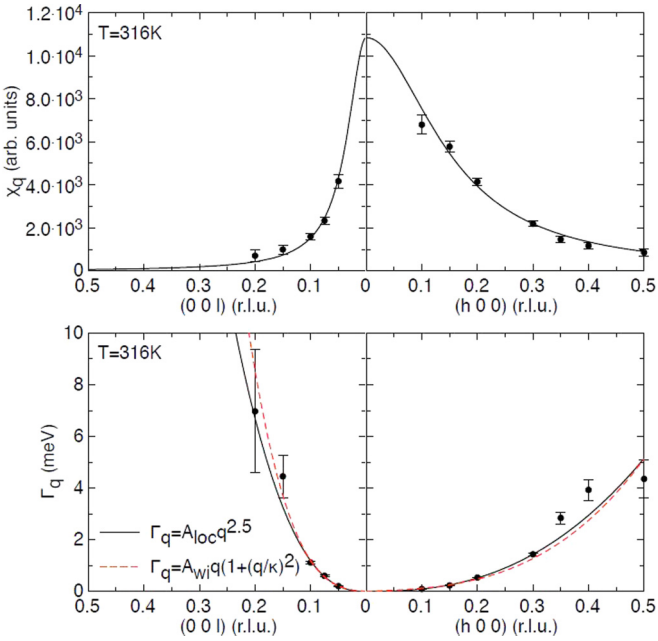

FIG. 8. q-dependent susceptibility χ_q (top) and linewidth Γ_q (bottom) in the (00l) and (h00) directions at 316 K. The solid black lines for χ_q correspond to Lorentzian fits as described in the text. The solid black and dashed red line for Γ_q correspond to the localized and weak itinerant model of ferromagnetism, respectively.

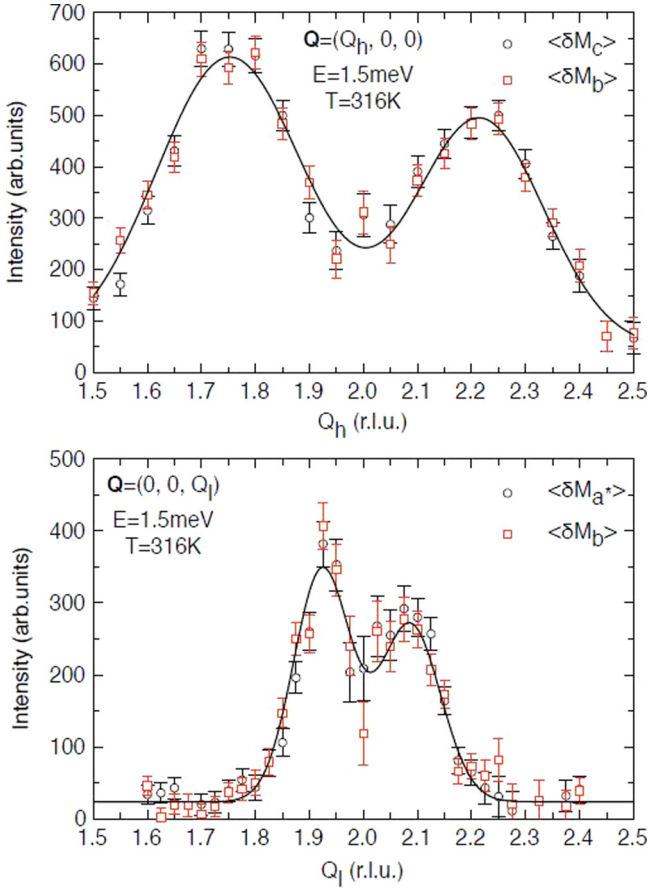

FIG. 9. Subtracted spin fluctuations spectra from constant energy scans at 1.5 meV at 316 K along (h00) (top) and (00l) (bottom) directions obtained at IN22. The indices i in $\langle \delta M_i \rangle$ indicates the direction of fluctuations (a^*, b, and c). Solid lines correspond to fits with Lorentzian functions.

models were used. For localized Heisenberg ferromagnets, the linewidth of the magnetic fluctuations can be expressed as $\Gamma_q = A_{\text{loc}} q^{2.5}$ [20]. On the other hand, for the weak itinerant model the expression is $\Gamma_q = A_{\text{wi}} q[1 + (q/\kappa)^2]$, where κ refers to the inverse correlation length [20]. The obtained values for the (00l) direction are $A_{\text{loc}} = 183(6)\,\text{meVÅ}^{2.5}$, $A_{\text{wi}} = 1.3(5)\,\text{meVÅ}$, and $\kappa_{(00l)} = 0.054(12)\,\text{Å}^{-1}$; for the (h00) direction $A_{\text{loc}} = 35.2(8)\,\text{meVÅ}^{2.5}$, $A_{\text{wi}} = 0.93(25)\,\text{meVÅ}$, and $\kappa_{(h00)} = 0.14(2)\,\text{Å}^{-1}$.

Constant energy scans were performed for an energy transfer of 1.5 meV along the directions (h00) and (00l) at 316 K in three non-spin flip channels NSF_{xx}, NSF_{yy}, and NSF_{zz} around the $\boldsymbol{\tau} = (2, 0, 0)$ and $\boldsymbol{\tau} = (0, 0, 2)$ zone centers. The in-plane and out-of-plane components of the magnetic fluctuations were separately obtained using canonical subtraction of intensities measured in the different polarization channels (see Appendix A). They are shown in Fig. 9. As can be seen, the in-plane $\langle \delta M_b \rangle$ and the out-of plane fluctuations $\langle \delta M_c \rangle$ are found to be isotropic (Fig. 9, top). The different in-plane components, $\langle \delta M_{a^*} \rangle$ and $\langle \delta M_b \rangle$, are also isotropic (Fig. 9, bottom). For this energy of 1.5 meV, the spectra show a maximum at a specific wave-vector $\mathbf{q} = (0.23, 0, 0)$ along (h00) and $\mathbf{q} = (0, 0, 0.08)$ along (00l)

direction, respectively. This mimics the spin-wave dispersion. However, the PM scattering is quasielastic, as can be seen in Fig. 7, since there is no well-defined inelastic mode associated with a given wave vector. Such "ridge" structure in (**Q**, E) space, i.e., maxima in constant-E spectra at finite q away from the Γ-point and maxima in constant-**Q** spectra for $E = 0$, is typical of PM scattering [20,21]. One can also see that the peak widths are very anisotropic between the basal plane, where a broad peak spans the whole Brillouin zone (Fig. 9, top) and perpendicular to the c axis, where a narrow peak shape is found (Fig. 9, bottom). The spectra measured at a constant energy of 1.5 meV were fitted by Lorentzian line shapes. The obtained effective inverse correlation lengths are $\kappa^*_{(h00)} = 0.139(2)\,\text{Å}^{-1}$ and $\kappa^*_{(00l)} = 0.0825(4)\,\text{Å}^{-1}$. They compare well with the correlation lengths obtained through the q dependence of the energy-integrated PM scattering (see above and Fig. 8).

V. DISCUSSION

Polarized and unpolarized INS measurements performed on single crystals of the MC compound $MnFe_4Si_3$ reveal a strong anisotropy in the exchange interactions between the (h00) and (00l) directions of the hexagonal system, while the magnetic fluctuations (dynamical susceptibilities) in the PM state at $T = 1.036T_C = 316\,\text{K}$ are found to be isotropic. This anisotropy is reflected in the magnon spectrum as well as in the q-dependent linewidths Γ_q (see Figs. 4 and 8). The ratio of the spin-wave stiffness D and the constant A_{loc} for the two directions is about of the same magnitude $(D_{(00l)}/D_{(h00)}) = 7.2(1.4)$ and $(A^{(00l)}_{\text{loc}}/A^{(h00)}_{\text{loc}}) = 5.2(2)$. The obtained data at 1.5 K indicate that the magnetic exchange interactions within the basal plane between the (h00) and (hh0) directions are isotropic. The experimental data collected at 1.5 K could be well described by a Heisenberg-type Hamiltonian. In the used effective spin-wave model, this translates into two FM exchange parameters with values $2SJ_2 = -18$ meV and $2SJ_1 = -4$ meV.

Strong anisotropy in the magnetic exchange interactions between the (h00) and (00l) directions has been reported for other FM compounds with hexagonal structure and lattice parameters comparable to $MnFe_4Si_3$, e.g., MnBi [22], MnSb [23,24], MnP [25,26] and Fe_2P [27]. Selected microscopic properties for representative hexagonal FM compounds are given in Table III. A striking feature is the large value of $D_{(00l)}$ and the related strong anisotropy for $MnFe_4Si_3$. For the isostructural MnT ferromagnets (T = Bi, Sb, P) decreasing the size of the T-ion leads to a decrease of interatomic Mn-Mn distance resulting in lower magnetic moments and Curie temperatures. This behavior might be attributed to a systematic shift from dominant itinerant to short-range exchange interactions with decreasing size of the T-ion [22]. In $MnFe_4Si_3$, the magnetic atoms that carry moments in WP $6g$, which has a mixed occupancy of Mn and Fe, have an interatomic shortest nearest neighbors distance of ≈2.775 Å comparable to MnP. This could hint to short range exchange magnetic interactions in $MnFe_4Si_3$.

Further insight can be gained from the calculation of the correlation lengths. The order of the FM transition is not clarified and since, experimentally, no discontinuity of the temperature dependence of magnetization was reported [9,12] and strong critical fluctuations are observed (Fig. 5), the inverse of the spin correlation length κ can be assumed to follow a critical law:

$$\kappa = \kappa_0 \left(\frac{|T - T_C|}{T_C} \right)^{\nu}. \tag{2}$$

In this formula, κ_0 refers to the inverse spin correlation length at 0 K and the exponent ν equals 0.5 and 0.7 for a Heisenberg model within the mean-field approximation and for critical scattering, respectively. The calculated values κ_0 for $\nu = 0.5$ result to: $\kappa_0^{(h00)} = 0.74(5)\,\text{Å}^{-1}$ and $\kappa_0^{(00l)} = 0.284(16)\,\text{Å}^{-1}$ and for $\nu = 0.7$ to: $\kappa_0^{(h00)} = 1.4(1)\,\text{Å}^{-1}$ and $\kappa_0^{(00l)} = 0.55(3)\,\text{Å}^{-1}$. One alternative model for calculating the inverse spin correlation lengths κ_0 by taking into account the spin-wave stiffness and the transition temperature is the following [21]:

$$\kappa_0 = \left(\frac{3k_B T_C}{(S+1)D} \right)^{0.5}, \tag{3}$$

which gives $\kappa_0^{(h00)} = 0.96(8)\,\text{Å}^{-1}$ and $\kappa_0^{(00l)} = 0.357(17)\,\text{Å}^{-1}$. These values are of the same order of magnitude as the ones obtained by Eq. (2). It is clearly seen that the corresponding correlation lengths $\xi_0 = \kappa_0^{-1}$ are smaller than the lattice parameters a and c, which points to a localized feature of the magnetism of $MnFe_4Si_3$. On the other hand, for itinerant magnetic systems ξ_0 are expected to be significantly larger [20,21].

Additional information can be given by the linewidths Γ_q. The experimental data for the Γ_q obtained at 316 K for the (h00) and (00l) directions could be well described both with a model for localized Heisenberg ferromagnets ($\Gamma_q = A_{\text{loc}} q^{2.5}$) as well as a model for weak itinerant ferromagnets ($\Gamma_q = A_{\text{wi}} q[1 + (q/\kappa)^2]$). The difficulty to distinguish between both models near T_C was reported previously for Ni_3Al [28].

The maximum value for Γ_q in the zone boundary ($q = 0.5$) for each direction is $\Gamma^{(h00)}_{\text{loc,max}} = 5.15(12)$ meV and $\Gamma^{(00l)}_{\text{loc,max}} = 62(2)$ meV, which means that the overall $\langle \Gamma_q \rangle$ is not expected to be higher than $2k_B T_C$. Based on the fact that the characteristic linewidths are higher than $k_B T_C$, we could expect an itinerant contribution to the magnetism. This is in agreement with Ref. [9], where the Rhodes-Wohlfarth model for the ratio of magnetic moments obtained from the Curie-Weiss law (M_c) to the low temperature saturation magnetization (M_s), $M_c/M_s = 1.7$ points to itinerant magnetism. To summarize, in our study, the obtained correlation lengths and linewidths point to both itinerant and localized contributions of the magnetism in the MC compound $MnFe_4Si_3$, a behavior typical of many ferromagnets [20].

Short-range magnetic correlations in the PM state were also observed in Fe_2P-based MC materials [31] and their importance for the MCE is not clearly demonstrated. However, our study shows that the temperature and the magnetic field ranges, where the change of entropy is sizable, matches the ones where the magnetic fluctuations are either critical (near T_C) or suppressed (near H = 2 T). This points to the importance of such fluctuations for the MCE. In particular, the critical scattering observed near T_C is strongly suppressed by a

TABLE III. Properties of selected ferromagnetic materials with hexagonal structure. Lattice parameters are given at around 300 K. M_s refers to the saturated magnetic moments. For MnP compound, the parameters are given in the distorted hexagonal NiAs-type structure. The lattice parameters for $MnFe_4Si_3$ are the ones obtained in the present study and are in agreement with Ref. [9].

Compound	T_C (K)	M_s μ_B	a (Å)	c (Å)	c/a	$D_{(h00)}$ (meVÅ^2)	$D_{(00l)}$ (meVÅ^2)	$D_{(00l)}/D_{(h00)}$	Easy axis of magnetization
Fe_2P [27,29,30]	209	1.46	5.88	3.44	0.585	42	76	1.81 (at 77 K)	c
MnP [25]	292	1.33	3.17	5.26	1.659	70	145	2.07 (at 150 K)	a
$MnFe_4Si_3$	305	1.5	6.78	4.72	0.696	43	310	7.2 (at 1.5 K)	b

magnetic field of 2 T. To get insight into the observed behavior, a comparison with the model of Ref. [19] has been performed. This model estimates the q-dependent susceptibility under a finite external magnetic field using the Landau theory for the magnetic fluctuations. The measurements shown in Fig. 6 probe the sum of the susceptibilities parallel and perpendicular to the field. In the vicinity of T_C, the expressions of Ref. [19] are given by:

$$\chi_q^{\parallel}(H,T_C) = \frac{\chi_q(0,T_C)}{1+\left(\frac{27}{30}\right)^{1/3}\left(\frac{\kappa_0}{q}\right)^2\left(\frac{g\mu_B H}{k_B T_C}\right)^{2/3}} \quad (4)$$

$$\chi_q^{\perp}(H,T_C) = \frac{\chi_q(0,T_C)}{1+\left(\frac{1}{30}\right)^{1/3}\left(\frac{\kappa_0}{q}\right)^2\left(\frac{g\mu_B H}{k_B T_C}\right)^{2/3}}. \quad (5)$$

The field-dependent susceptibility is calculated by inserting the parameters obtained above for $\nu = 0.5$ and by averaging the in- and out-of-plane correlation lengths (giving $(\frac{\kappa_0}{q})^2 \approx 100$). The obtained calculation is shown in the inset of Fig. 6 with an overall scale factor as the only free parameter. The calculated function describes qualitatively well the data, but the observed decrease with magnetic field is quantitatively stronger. Such disagreement could be attributed to different reasons: the finite integration in energy of our data ($-0.1 \leqslant E \leqslant 0.1$ meV), the isotropic nature of spin correlations in the model of Ref. [19], or a fluctuations pattern beyond the Landau theory. Since such studies on the effect of a magnetic field on the critical fluctuations are scarce, it is difficult to draw firm conclusions. The same model was used to describe the suppression of the critical fluctuations in Gd [32] and here also the agreement is semiqualitative. In this context, further studies on the effect of the magnetic field on the magnetic critical fluctuations are necessary regarding their potential importance for the MCE.

VI. CONCLUSION

Our detailed study of the spin dynamics of the MC compound $MnFe_4Si_3$ provides key microscopic information concerning the nature of the magnetism in this system. Among the specific features highlighted in the present study are the isotropic dynamical spin susceptibilities in the PM state, strong anisotropy between in- and out-of-plane magnetic exchange interactions, short-range correlation lengths compared to typical distances, and extended characteristic linewidths compared to T_C. So far it is not clear which ingredient is favorable to produce a large MCE. Our study suggests that the strong response of the critical fluctuations in the PM state to a magnetic field of 2 T is an important feature. Thus a systematic study of the spin dynamics of various MC compounds to highlight the major components at play and to finally optimize the materials in view of applications is highly needed.

APPENDIX A: POLARIZED NEUTRON MEASUREMENTS

For polarized neutron experiments, the usual convention is to define a cartesian coordinate system with the x axis parallel to $\mathbf{Q}$, the y axis perpendicular to $\mathbf{Q}$ in the scattering plane, and the z axis perpendicular to the scattering plane. Since neutron scattering experiments probe only the magnetism perpendicular to the scattering vector $\mathbf{Q}$, the measured magnetic fluctuations are therefore $\langle \delta M_y \rangle$ and $\langle \delta M_z \rangle$, where

$$\langle \delta M_\beta \rangle = \frac{1}{2\pi}\int \langle \delta M(-Q)_\beta^{\perp}(0)\delta M(Q)_\beta^{\perp}(t)\rangle e^{-i\omega t}dt. \quad (A1)$$

$\delta M(Q)_\beta^{\perp}(t)$ is the β component of the Fourier component of the magnetic fluctuations perpendicular to $\mathbf{Q}$ and $\langle ... \rangle$ is the quantum statistical expectation value.

In our experiments, longitudinal polarization analysis was performed: the initial polarization of the neutron beam $\mathbf{P}$ lies along x, y, or z and only the scattering events where the final polarization lies either parallel—non-spin flip channel (NSF)—or antiparallel—spin flip channel (SF)—to $\mathbf{P}$ are measured. Magnetic fluctuations parallel to $\mathbf{P}$ give rise to NSF scattering and magnetic fluctuations perpendicular to $\mathbf{P}$ give rise to SF scattering. Given the high polarization, no polarization corrections were applied to the data.

1. Spin-wave scattering

The polarization is along the direction of the applied vertical magnetic field, z, which corresponds to the direction of the ordered magnetic moments in the single domain sample. Spin waves correspond to precession perpendicular to the ordered moment with, therefore, a unique component $\langle \delta M_y \rangle$. The neutron scattering double differential cross sections are:

$$\mathrm{NSF}_{zz} : \left(\frac{d^2\sigma}{d\Omega dE}\right)^z_{\mathrm{NSF}} \propto BG_{\mathrm{NSF}} + \langle N \rangle \quad (A2)$$

$$\mathrm{SF}_{zz} : \left(\frac{d^2\sigma}{d\Omega dE}\right)^z_{\mathrm{SF}} \propto BG_{\mathrm{SF}} + \langle \delta M_y \rangle \quad (A3)$$

where $\langle N \rangle$ is the nuclear scattering and BG_{NSF} and BG_{SF} are the background in the NSF and SF channel, respectively. In the crystal frame and for $\mathbf{Q}$ in the (a*,c) plane, the cross sections

become:

$$\left(\frac{d^2\sigma}{d\Omega dE}\right)^z_{\rm NSF} \propto BG_{\rm NSF} + \langle N\rangle \quad \text{(A4)}$$

$$\left(\frac{d^2\sigma}{d\Omega dE}\right)^z_{\rm SF} \propto BG_{\rm SF} + \cos^2\theta\langle\delta M_c\rangle + \sin^2\theta\langle\delta M_{a^*}\rangle \quad \text{(A5)}$$

with θ the angle between $\mathbf{Q}$ and the (h00) direction.

2. Paramagnetic scattering

In this part, NSF scattering was measured with the double differential cross-sections:

$$\text{NSF}_{xx}: \left(\frac{d^2\sigma}{d\Omega dE}\right)^x_{\rm NSF} \propto BG_{\rm NSF} + \langle N\rangle \quad \text{(A6)}$$

$$\text{NSF}_{yy}: \left(\frac{d^2\sigma}{d\Omega dE}\right)^y_{\rm NSF} \propto BG_{\rm NSF} + \langle N\rangle + \langle\delta M_y\rangle \quad \text{(A7)}$$

$$\text{NSF}_{zz}: \left(\frac{d^2\sigma}{d\Omega dE}\right)^z_{\rm NSF} \propto BG_{\rm NSF} + \langle N\rangle + \langle\delta M_z\rangle. \quad \text{(A8)}$$

For scattering vectors $\mathbf{Q}$ parallel to (h00), the scattering cross sections are for (a*,c) plane:

$$\left(\frac{d^2\sigma}{d\Omega dE}\right)^x_{\rm NSF} \propto BG_{\rm NSF} + \langle N\rangle \quad \text{(A9)}$$

$$\left(\frac{d^2\sigma}{d\Omega dE}\right)^y_{\rm NSF} \propto BG_{\rm NSF} + \langle N\rangle + \langle\delta M_c\rangle \quad \text{(A10)}$$

$$\left(\frac{d^2\sigma}{d\Omega dE}\right)^z_{\rm NSF} \propto BG_{\rm NSF} + \langle N\rangle + \langle\delta M_b\rangle. \quad \text{(A11)}$$

It is possible to determine $\langle\delta M_c\rangle$ and $\langle\delta M_b\rangle$ by making the subtraction Eqs. (A10)–(A9) and Eqs. (A11)–(A9), respectively. For scattering vectors $\mathbf{Q}$ parallel to (00l), the scattering cross sections are for (a*,c) plane:

$$\left(\frac{d^2\sigma}{d\Omega dE}\right)^x_{\rm NSF} \propto BG_{\rm NSF} + \langle N\rangle \quad \text{(A12)}$$

$$\left(\frac{d^2\sigma}{d\Omega dE}\right)^y_{\rm NSF} \propto BG_{\rm NSF} + \langle N\rangle + \langle\delta M_{a^*}\rangle \quad \text{(A13)}$$

$$\left(\frac{d^2\sigma}{d\Omega dE}\right)^z_{\rm NSF} \propto BG_{\rm NSF} + \langle N\rangle + \langle\delta M_b\rangle. \quad \text{(A14)}$$

It is possible to determine $\langle\delta M_{a^*}\rangle$ and $\langle\delta M_b\rangle$ by making the subtraction Eqs. (A13)–(A12) and Eqs. (A14)–(A12), respectively.

APPENDIX B: SCATTERING FUNCTIONS

The measured intensity $I(\mathbf{Q},\omega)$ is the convolution of the resolution function $F(\mathbf{Q},\omega)$ and the scattering function $S(\mathbf{Q},\omega)$: $I(\mathbf{Q},\omega) = F(\mathbf{Q},\omega) \otimes S(\mathbf{Q},\omega)$. In this paper, the constant $\mathbf{Q}$ spectra at T = 316 K were convoluted with a one-dimensional resolution in the ω direction. We assumed that the resolution function has a Gaussian shape with widths defined from measurements on a vanadium sample. The scattering function and the imaginary part of the dynamical spin susceptibility $\chi''(\mathbf{Q},\omega)$ are connected through the following relation:

$$S(\mathbf{Q},\omega) = \frac{1}{1-e^{-\omega/T}}\chi''(\mathbf{Q},\omega), \quad \text{(B1)}$$

where ω and T are given in units of $\hbar$ and k_B, respectively. The paramagnetic scattering can be described with the Lorentzian-like equation $\chi''(\mathbf{q},\omega)$:

$$\chi''(\mathbf{q},\omega) = \frac{\chi_0}{1+(q/\kappa)^2}\frac{\omega\Gamma_q}{\omega^2+\Gamma_q^2} = \chi_q\frac{\omega\Gamma_q}{\omega^2+\Gamma_q^2}, \quad \text{(B2)}$$

where χ_q, Γ_q, and κ are the q-dependent susceptibility, linewidth, and inverse correlation length and χ_0 the static susceptibility. For all the obtained constant $\mathbf{Q}$ spectra at $1.036T_C \approx 316$ K (e.g., Fig. 7) the energy transfer was between $-5 \leqslant E \leqslant 5$ meV. For this energy range and temperature, Eq. (B1) combined with Eq. (B2) is simplified to the double Lorentzian form:

$$S(\mathbf{q},\omega) = T\frac{\chi_0}{1+(q/\kappa)^2}\frac{\Gamma_q}{\omega^2+\Gamma_q^2} = T\chi_q\frac{\Gamma_q}{\omega^2+\Gamma_q^2}. \quad \text{(B3)}$$

The resulting fit for the measured intensity $I(\mathbf{Q},\omega)$ can be realized as a Voigt function. From the Voigt's function amplitude χ_q can be extracted and the width of the Lorentzian part (HWHM) corresponds to Γ_q. The width of the Gaussian part is fixed to a constant value, defined from the vanadium sample measurement.

[1] K. A. Gschneidner, Jr. and V. K. Pecharsky, Int. J. Refrig. **31**, 945 (2008).

[2] O. Tegus, E. Brück, K. H. J. Buschow, and F. R. de Boer, Nature **415**, 150 (2002).

[3] G. V. Brown, J. Appl. Phys. **47**, 3673 (1976).

[4] V. K. Pecharsky and K. A. Gschneidner, Jr., Phys. Rev. Lett. **78**, 4494 (1997).

[5] O. Tegus, E. Brück, L. Zhang, Dagula, K. H. J. Buschow, and F. R. de Boer, Phys. B **319**, 174 (2002).

[6] N. H. Dung, Z. Q. Ou, L. Caron, L. Zhang, D. T. Cam Thanh, G. A. de Wijs, R. A. de Groot, K. H. J. Buschow, and E. Brück, Adv. Energy Mater. **1**, 1215 (2011).

[7] Songlin, Dagula, O. Tegus, E. Brück, J. C. P. Klaasse, F. R. de Boer, and K. H. J. Buschow, J. Alloys Compd. **334**, 249 (2002).

[8] H. Bińczycka, Z. Dimitrijević, B. Gajić, and A. Szytula, Phys. Status Solidi **19**, K13 (1973).

[9] P. Hering, K. Friese, J. Voigt, J. Persson, N. Aliouane, A. Grzechnik, A. Senyshyn, and T. Brückel, Chem. Mater. **27**, 7128 (2015).

[10] A. Candini, O. Moze, W. Kockelmann, J. M. Cadogan, E. Brück, and O. Tegus, J. Appl. Phys. **95**, 6819 (2004).

[11] O. Gourdon, M. Gottschlich, J. Persson, C. de la Cruz, V. Petricek, M. A. McGuire, and T. Brückel, J. Solid State Chem. **216**, 56 (2014).

[12] M. Herlitschke, B. Klobes, I. Sergueev, P. Hering, J. Persson, and R. P. Hermann, Phys. Rev. B **93**, 094304 (2016).
[13] M. F. J. Boeije, M. Maschek, X. F. Miao, N. V. Thang, N. H. van Dijk, and E. Brück, J. Phys. D: Appl. Phys. **50**, 174002 (2017).
[14] K. Schmalzl, W. Schmidt, S. Raymond, H. Feilbach, C. Mounier, B. Vettard, and T. Brückel, Nucl. Instrum. Methods A **819**, 89 (2016).
[15] H. M.-L. Zentrum *et al.*, J. Large-Scale Res. Facil. **1**, A3 (2015).
[16] H. M.-L. Zentrum *et al.*, J. Large-Scale Res. Facil. **1**, A13 (2015).
[17] In this paper: $\mathbf{Q} = \boldsymbol{\tau} + \mathbf{q}$, where $\boldsymbol{\tau}$ corresponds to a zone center, $\mathbf{Q} = (Q_h, Q_k, Q_l)$ is the scattering vector and $\mathbf{q} = (h,k,l)$ expresses the wave vector of an elementary excitation expressed in reciprocal lattice units. All vectors are expressed in hexagonal coordinates.
[18] S. Petit and F. Damay, Neutron News **27**, 27 (2016).
[19] J. Villain, J. Phys. (France) **24**, 622 (1963).
[20] Y. Endoh and P. Böni, J. Phys. Soc. Jpn. **75**, 111002 (2006).
[21] T. Moriya, Springer Ser. Solid-State Sci. **56**, 194 (1985).
[22] T. J. Williams, A. E. Taylor, A. D. Christianson, S. E. Hahn, R. S. Fishman, D. S. Parker, M. A. McGuire, B. C. Sales, and M. D. Lumsden, Appl. Phys. Lett. **108**, 192403 (2016).
[23] Y. Yamaguchi, S. Tomoyoshi, M. Harada, and G. Shirane, J. Magn. Magn. Mater. **103**, 50 (1992).
[24] P. Radhakrishna and J. W. Cable, Phys. Rev. B **54**, 11940 (1996).
[25] Y. Todate, K. Yamada, Y. Endoh, and Y. Ishikawa, J. Phys. Soc. Jpn. **56**, 36 (1987).
[26] S. Yano, S. Itoh, T. Yokoo, S. Satoh, D. Kawana, Y. Kousaka, J. Akimitsu, and Y. Endoh, J. Magn. Magn. Mater. **347**, 33 (2013).
[27] S. Komura, K. Tajima, H. Fujii, Y. Ishikawa, and T. Okamoto, J. Magn. Magn. Mater. **15–18**, 351 (1980).
[28] F. Semadeni, B. Roessli, P. Böni, P. Vorderwisch, and T. Chatterji, Phys. Rev. B **62**, 1083 (2000).
[29] H. Fujii, Y. Uwatoko, K. Motoya, Y. Ito, and T. Okamoto, J. Phys. Soc. Jpn. **57**, 2143 (1988).
[30] C. Wilkinson, R. Wäppling, and K. R. A. Ziebeck, J. Magn. Magn. Mater. **78**, 269 (1989).
[31] X. F. Miao, L. Caron, J. Cedervall, P. C. M. Gubbens, P. Dalmas de Réotier, A. Yaouanc, F. Qian, A. R. Wildes, H. Luetkens, A. Amato, N. H. van Dijk, and E. Brück, Phys. Rev. B **94**, 014426 (2016).
[32] J. W. Cable and R. M. Nicklow, J. Phys.: Condens. Matter **1**, 7425 (1989).